

# On the Eutectoid Reaction in a Quaternary Fe-C-Mn-Al Alloy: Austenite $\rightarrow$ Ferrite + Kappa-Carbide + $M_{23}C_6$ Carbide

WEI-CHUN CHENG, YUAN-SHENG SONG, YU-SHAN LIN, KUAN-FU CHEN,  
and PETRUS C. PISTORIUS

Lamellae of ferrite, kappa-carbide, and  $M_{23}C_6$  carbide are involved in a eutectoid reaction of an Fe-C-Mn-Al alloy after isothermal holding at temperatures below 923 K (650 °C). These lamellar phases are product phases from the decomposition of austenite during the eutectoid reaction of the quaternary alloy, *i.e.*, austenite  $\rightarrow$  ferrite + kappa-carbide +  $M_{23}C_6$  carbide. Since the Al concentration in the steel is higher than that of the eutectoid composition, proeutectoid ferrite and kappa-carbide appear in the austenite prior to the eutectoid reaction to reduce the Al content of the retained austenite. The retained austenite decomposes into ferrite, kappa-carbide, and  $M_{23}C_6$  carbide during the eutectoid reaction.

DOI: 10.1007/s11661-013-2083-2

© The Minerals, Metals & Materials Society and ASM International 2013

## I. INTRODUCTION

WHEN a binary Fe-C steel of eutectoid composition, containing about 0.77 wt pct C, is cooled below the eutectoid temperature at constant pressure, the invariant reaction of the eutectoid transformation takes place: austenite  $\rightarrow$  ferrite +  $Fe_3C$ . The product phases of the eutectoid reaction form pearlite comprising lamellar ferrite and  $Fe_3C$  (cementite). The pearlite colonies nucleate preferentially at the original austenite grain boundaries and grow into the austenite matrix. For steels with greater or lesser carbon contents than the eutectoid composition, cooled slowly or held isothermally below the eutectoid temperature, the appearance of pearlite is usually preceded by the precipitation of proeutectoid cementite or ferrite, respectively, at the grain boundaries prior to the eutectoid reaction.<sup>[1]</sup> For austenite cooled well below the eutectoid temperature, for example, in the bainite formation region of a time-temperature-transformation (TTT) diagram, different eutectoid products are produced. Bainite is a mixture of ferrite and carbide similar to pearlite, but it is microstructurally quite distinct from pearlite. Usually, bainite forms with the leading phase of Widmanstätten ferrite in the main growth direction. Thus, bainite is favored in low carbon steels. Inverse bainite with ferrite plates attached to Widmanstätten cementite plates is the major phase in the austenite matrix of hypereutectoid steels at low temperatures.<sup>[2–8]</sup> Lee *et al.* made a distinction

between cooperative and non-cooperative eutectoid reactions in terms of relative growth rates of the product phase. The formation of pearlite is in the category of cooperative (lamellar) eutectoid reactions and that of bainite is in the category of non-cooperative (non-lamellar) eutectoid transformations.<sup>[9]</sup>

Various phase transformations of ternary alloys under constant pressure conditions have been well illustrated by Rhines.<sup>[10]</sup> Invariant reactions for four-phase equilibrium are categorized as class I, II, and III. For example, Class I involves the ternary eutectic reaction: the decomposition of liquid into three different solid phases at the eutectic temperature. The class I invariant reaction of the eutectic transformations has been well documented in the solidification literature. Some published micrographs have illustrated that the ternary class I eutectic reaction products consist of two continuous major phases and an apparently discontinuous minor product phase in such systems as Cd-Sn-(Pb, In, Tl), Al-Cu-(Mg, Zn, Ag), and Zn-Sn-Pb.<sup>[11]</sup> The three four-phase equilibria are also applicable to solid-state phase transformations, such as the eutectoid reaction, and the extension is most likely pertinent to phase transformations in quaternary alloy systems.

Another pearlite with lamellae of ferrite and  $M_{23}C_6$  carbide, called  $M_{23}C_6$  pearlite, has been found in alloy steels, for example, in Fe-C-Cr alloys<sup>[12,13]</sup> and in Fe-C-Mn-Al alloys.<sup>[14,15]</sup> Instead of  $M_3C$  plates, lamellar  $M_{23}C_6$  carbide grains are embedded in the ferrite matrix of the  $M_{23}C_6$  pearlite. The partitioning of Mn, Al, and C solutes is distinct in the  $M_{23}C_6$  pearlite of the Fe-C-Mn-Al alloy. The  $M_{23}C_6$  carbide contains a high concentration of Mn and C and a low concentration of Al, whereas the ferrite has a high concentration of Al and a low concentration of Mn and C.<sup>[14,15]</sup> Similar experimental observations have also been reported for the partitioning of Mn and C solutes in the lamellar ferrite and  $M_3C$  which comprise  $M_3C$  pearlite in high Mn steels. The  $M_3C$  carbide contains a high concentration

WEI-CHUN CHENG, Professor, and YUAN-SHENG SONG, YU-SHAN LIN, and KUAN-FU CHEN, Graduate Students, are with the Department of Mechanical Engineering, National Taiwan University of Science and Technology, 43 Keelung Road, Section 4, Taipei 106, Taiwan, R.O.C. Contact e-mail: weicheng@mail.ntust.edu.tw PETRUS C. PISTORIUS, Professor, is with the Department of Materials Science and Engineering, Carnegie Mellon University, 5000 Forbes Ave., Pittsburgh, PA.

Manuscript submitted February 5, 2013.

Article published online November 2, 2013

of Mn and C, and the ferrite has a low concentration of Mn and C.<sup>[16,17]</sup>

Phase equilibria of Fe-C-Al alloys close to the Fe corner, at constant pressure, have been studied for several decades.<sup>[18–20]</sup> These alloys with low carbon contents are characterized by a wide solid solution of body-centered cubic (BCC) ferrite. However, when these alloys have high carbon concentrations, they contain face-centered cubic (FCC) austenite, cementite, and a ternary perovskite carbide, which is denoted as kappa-carbide ( $\kappa$ -carbide).<sup>[18]</sup> In ternary Fe-C-Al alloys, ferrite, austenite, cementite, and  $\kappa$ -carbide are high-temperature phases. The phase transitions of quaternary Fe-C-Mn-Al alloys have been investigated for several decades.<sup>[21–37]</sup>

Besides the  $\kappa$ -carbide, the  $L_{12}$  phase precipitates homogeneously in the austenite of these alloys. The  $L_{12}$  phase is a derivative phase of the austenite. In 1990, Ishida *et al.*<sup>[31]</sup> established several isothermal phase diagrams of quaternary Fe-C-Mn-Al alloys. The isothermal sections of the phase diagrams of the steels, for example, at fixed 20 wt pct Mn, are shown in Figure 1. The high-temperature phases, which include ferrite, austenite, cementite, and  $\kappa$ -carbide, are similar to those of the ternary Fe-C-Al alloys. Two-phase fields of (ferrite + austenite), (ferrite +  $\kappa$ -carbide), and (austenite +  $\kappa$ -carbide) and even a three-phase field of (ferrite + austenite +  $\kappa$ -carbide) exist in the quaternary Fe-C-Mn-Al alloys. Similar phase diagrams of quaternary Fe-C-Mn-Al alloys were also published by Gorev *et al.* in 1990.<sup>[38]</sup>

We have studied the phase transformations of quaternary Fe-C-Mn-Al alloys under a constant pressure of 1 atm.<sup>[14,15,32–37]</sup> Aside from the discovery of  $M_{23}C_6$  pearlite in a few Fe-C-Mn-Al alloys,<sup>[14,15]</sup> we have found lamellae of ferrite and  $\kappa$ -carbide in some Fe-C-Mn-Al alloys. In addition, we have discovered lamellar  $M_{23}C_6$  carbide grains appearing in the lamellae of ferrite and  $\kappa$ -carbide of an Fe-C-Mn-Al alloy. Here, we report that ferrite,  $\kappa$ -carbide, and  $M_{23}C_6$  carbide are product phases of the eutectoid reaction of the quaternary Fe-C-Mn-Al alloy.

## II. EXPERIMENTAL PROCEDURES

Slabs with a composition of Fe-13.5 Mn-6.3 Al-0.78 C (wt pct) were initially prepared by induction melting. Commercial 1020 steel, carbon, electrolytic manganese, and high purity aluminum were melted together and cast into 3-kg ingots. After being homogenized at 1473 K (1200 °C) for 4 hours under a protective argon atmosphere, the ingots were hot forged and annealed to insure composition uniformity of the steel plates. The steel plates were cold rolled to thin plates with a thickness of 2 mm and cut into specimens with dimensions of 15 mm × 10 mm. The steel samples were heated at 1373 K (1100 °C) for 1 hour in a protective argon atmosphere and quenched in water at room temperature for solution heat treatment. The measured composition of the minor elements of the steel plates in wt pct is 0.00 Si-0.01 P-0.01 S. The as-quenched specimens were sealed in quartz tubes under vacuum and held isothermally at low temperatures ranging from 1123 K to 773 K (850 °C to 500 °C) for 100 hours.

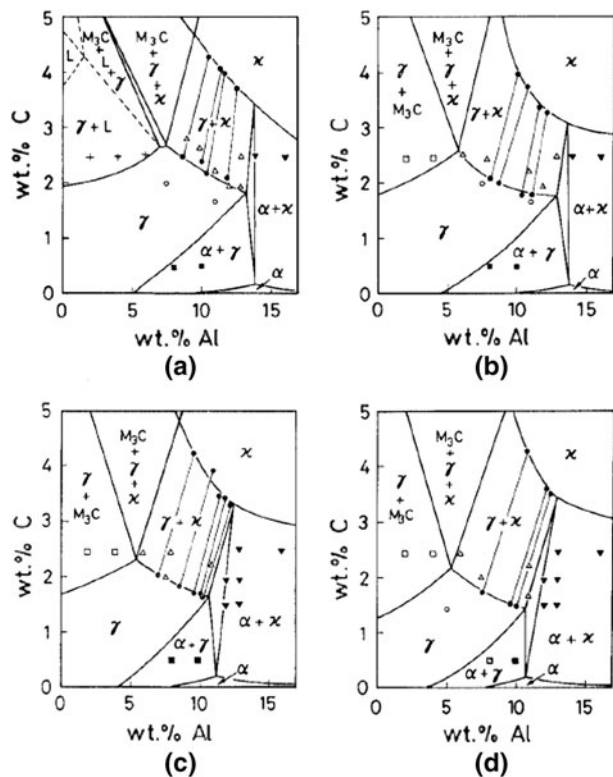


Fig. 1—(a) through (d) The isothermal phase diagrams of Fe-C-Mn-Al alloys at fixed 20 wt pct Mn. The temperatures are indicated as follows: (a) 1473 K, (b) 1373 K, (c) 1273 K, and (d) 1173 K.<sup>[32]</sup>

The samples were sectioned, polished mechanically, and etched in a 5 pct nital solution for observation under an optical microscope and a Jeol JEM 6500F high resolution field-emission scanning electron microscope (SEM). Some samples were also examined by X-ray diffraction (XRD) in a Rigaku DMAX-B X-ray diffractometer operated at a power of 12 kW. Samples used for observation by transmission electron microscopy (TEM) were polished mechanically into thin foils about 80  $\mu\text{m}$  in thickness, punched into circles with a diameter of 3 mm, and then electropolished using a twin jet polisher in a 90 pct  $\text{CH}_3\text{COOH}$  and 10 pct  $\text{HClO}_4$  solution at room temperature. The samples also underwent ion milling in an ion miller to polish the thin areas of the TEM specimens. The samples were examined in a Jeol JEM 2010 transmission electron microscope equipped with a Link ISIS 300 energy-dispersive X-ray analyzer (EDS) operated at 200 kV. The EDS uses the quantitative method of Cliff–Lorimer Ratio Thin Section. The tilt angles of the specimens in TEM are  $\pm 45$  and  $\pm 34$  deg in the  $x$ - and  $y$ -axis, respectively.

## III. RESULTS AND DISCUSSION

### A. Phase Diagrams of the Fe-Mn-Al Alloy

Figures 2(a) through (d) show the calculated partial phase diagrams of the quaternary Fe-C-Mn-Al alloy with a fixed 13.5 wt pct Mn, carbon content lower than

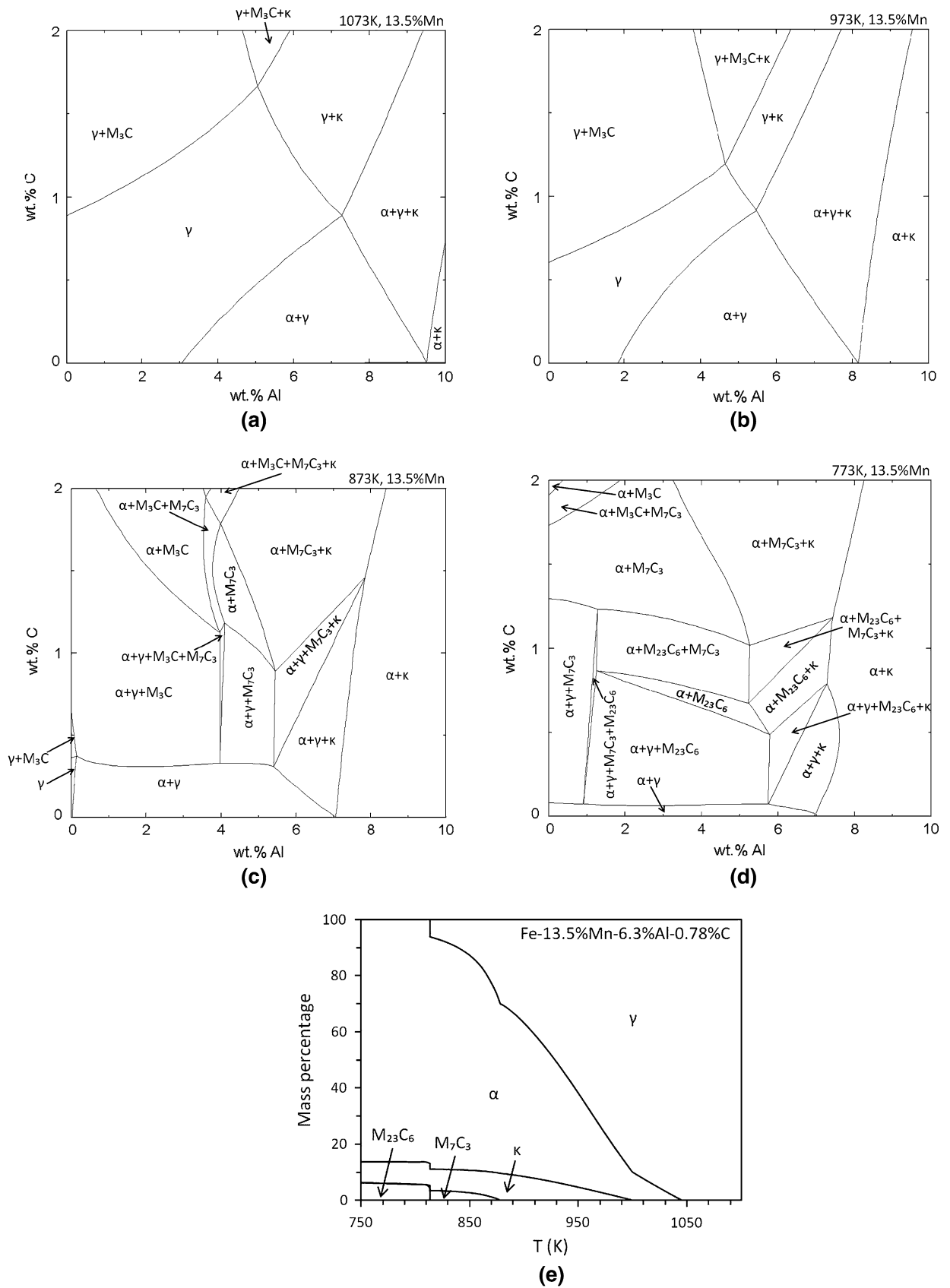


Fig. 2—Calculated phase diagrams of the quaternary Fe-C-Mn-Al alloy with a fixed 13.5 wt pct Mn. The temperatures for the partial isothermal sections of the phase diagram in (a) through (d) are (a) 1073 K, (b) 973 K, (c) 873 K, and (d) 773 K. (e) The calculated effect of temperature on the equilibrium phase proportions in the Fe-13.5Mn-6.3Al-0.78C alloy.

2 wt pct, and Al content lower than 10 wt pct. The temperatures for the isothermal sections of the phase diagram in Figures 2(a) through (d) are (a) 1073 K (800 °C), (b) 973 K (700 °C), (c) 873 K (600 °C), and (d) 773 K (500 °C). The FactSage 6.4 software was used to calculate the diagram, using the FSstel database, and suppressing graphite formation.<sup>[39]</sup> Figure 2(e) is the calculated effect of temperature on the equilibrium phase proportions in the Fe-13.5 Mn-6.3 Al-0.78 C alloy. Figure 2(a) shows that the high-temperature phase diagram at 1073 K is slightly different from the experimentally determined high-temperature phase diagrams with a fixed composition of 20 wt pct Mn, as shown in Figure 1. The high-temperature phases of the quaternary Fe-C-Mn-Al alloys include austenite, ferrite, cementite, and  $\kappa$ -carbide. Figure 2(b) predicts the phases of the alloy systems at 973 K (700 °C). Shrinkage of the austenite and expansion of other two-phase fields have been observed.  $M_7C_3$  carbide appears in the phase diagrams at temperatures of 873 K and 773 K (600 °C and 500 °C) as shown in Figures 2(c) and (d), respectively.  $M_{23}C_6$  carbide appears in the phase diagram at 773 K (500 °C) as shown in Figure 2(d). Thus,  $M_7C_3$  and  $M_{23}C_6$  carbides are low-temperature phases in the Fe-C-Mn-Al alloy. According to the phase proportions in Figure 2(e), the Fe-0.78C-13.5 Mn-6.3 Al alloy is fully austenitic at 1073 K (800 °C). Upon lowering the temperature from 1073 K (800 °C), the constituent phases of the Fe-C-Mn-Al alloy change as follows: austenite  $\rightarrow$  austenite + ferrite  $\rightarrow$  austenite + ferrite +  $\kappa$ -carbide  $\rightarrow$  austenite + ferrite +  $\kappa$ -carbide +  $M_7C_3$  carbide  $\rightarrow$  ferrite +  $\kappa$ -carbide +  $M_{23}C_6$  carbide.

### B. Austenite at 1373 K (1100 °C)

An optical micrograph (OM) of the Fe-C-Mn-Al alloy after solution heat treatment at 1373 K (1100 °C) is shown in Figure 3(a). Similar grains with annealing twins indicate that the alloy is single phase in both high-temperature and as-quenched conditions. Figure 3(b) shows an XRD analysis for the steel in the as-quenched

condition. Only FCC austenite peaks were detected by the XRD in Figure 3(b). Thus, the high-temperature phase of the steel at 1373 K (1100 °C) is austenite. The austenite has also been preserved as the only phase in the as-quenched condition. After identifying the constituent phase of the steel in the as-quenched condition, we further studied the low-temperature phases of the steel after the following isothermal holding processes. For the steel samples held at temperatures of 1123 K and 1098 K (850 °C and 825 °C), no precipitates were discovered in the austenite by OM, XRD, and TEM analyses, which are not shown here. Thus, the steel consists of single-phase austenite at temperatures from 1373 K to 1098 K (1100 °C to 825 °C).

### C. Austenite $\rightarrow$ Austenite + Ferrite + $\kappa$ -Carbide

The OM and TEM analyses of the steel after solution heat treatment and 100-hour isothermal holding at 973 K (700 °C) are revealed in Figure 4. The OM in Figure 4(a) reveals a continuous distribution of precipitates along almost all the austenite grain boundaries. A TEM bright-field (BF) image in Figure 4(b) illustrates that several different phase grains appear at the grain boundary. Some grains are marked with  $\alpha$ , other grains are labeled  $\kappa$ , and a third type of grain is the matrix phase austenite marked  $\gamma$ . Figure 4(c) is the corresponding selected area diffraction (SAD) pattern of the big  $\alpha$ -grain in the center running to the upper-right-hand side. We identified the  $\alpha$ -grain as BCC ferrite. The zone axis of the SAD pattern from the ferrite in Figure 4(c) is in the  $[\bar{1}11]$  direction. The  $\kappa$ -grains have a simple cubic crystal structure and were confirmed to be  $\kappa$ -carbide. The SAD pattern, taken from the  $[0\bar{1}1]$  zone-axis direction of the  $\kappa$ -carbide, is shown in Figure 4(d). The constituent phases of the steel at 973 K (700 °C) and other temperatures are summarized in Table I. We found grain boundary ferrite precipitates in the austenite after isothermal holding at 1073 K (800 °C), and separate grains of ferrite and  $\kappa$ -carbide appear at the

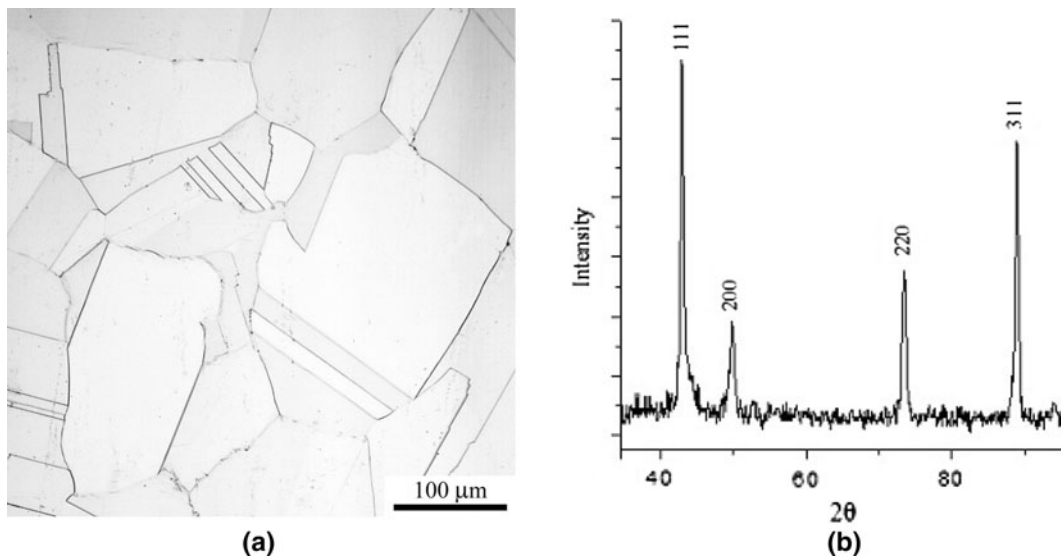


Fig. 3—(a) The OM and (b) XRD analyses of the steel after the solution heat treatment at 1373 K.

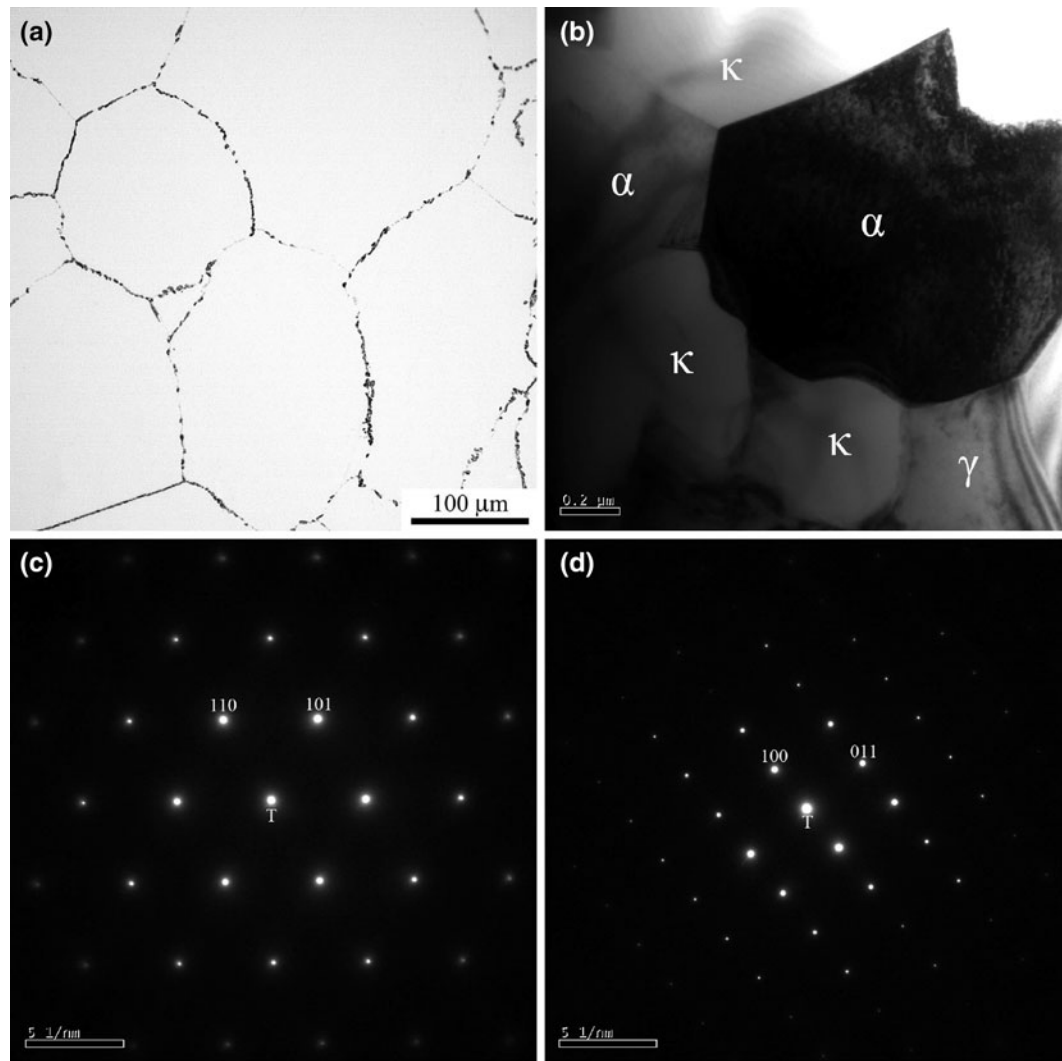


Fig. 4—The OM and TEM analyses of the steel after isothermal holding at 973 K for 100 h. (a) The OM and (b) BF image showing the grain boundary precipitates in the austenite ( $\alpha$ : ferrite;  $\kappa$ :  $\kappa$ -carbide;  $\gamma$ : austenite). (c) The SAD pattern from  $[\bar{1}11]$  ferrite (T: transmission beam). (d) The SAD pattern taken at  $[0\bar{1}1]$   $\kappa$ -carbide.

**Table I. The Constituent Phases of the Fe-C-Mn-Al Alloy at Different Isothermal Holding Temperatures.  $\alpha$  (Ferrite) and  $\kappa$  ( $\kappa$ -Carbide) are Grain Boundary Precipitates**

$T$ [K (°C)]	Phase			
	$\alpha$	$\kappa$	$\alpha + \kappa$	$M_{23}C_6$
1098 (795)				
1073 (1050)	●			
1023 (750)	●	●		
973 (700)	●	●		
948 (675)			●	
923 (650)		●	●	
898 (625)			●	●
873 (600)			●	●
848 (575)			●	●
823 (550)			●	●
773 (500)			●	

( $\alpha + \kappa$ ) means the  $\kappa$ -pearlite. The isothermal holding time is 100 h.

grain boundaries for steel held at 1023 K (750 °C). The experimental observation is quite similar to that predicted by the calculated phase diagrams, except for the appearance of the second phases, ferrite and  $\kappa$ -carbide, at higher temperature (1073). The chemical compositions of the phases were analyzed by EDS, which is standard equipment in the TEM. Because of carbon contamination on the surface of the TEM specimen, no carbon measurement from the EDS signal was made. The chemical compositions of the constituent phases in the metallic portion in weight percent (atomic percent in parentheses) of the phases at 973 K (700 °C) are as follows. The austenite matrix contains Fe-15.0 Mn-4.6 Al (Fe-14.6 Mn-9.1 Al), the composition of the ferrite is Fe-7.0 Mn-6.0 Al (Fe-6.7 Mn-11.7 Al), and that of the  $\kappa$ -carbide is Fe-23.0 Mn-8.9 Al (Fe-22.2 Mn-15.9 Al). As the EDS utilizes the Cliff-Lorimer Ratio Thin Section quantitative method, the error in Fe is about 0.25 pct, Mn 1.0 pct, and Al 10 pct. The chemical compositions of

**Table II. The Compositions of Constituent Phases in the Metallic Portion Analyzed by TEM-EDS—(a) Weight Percentage and (b) Atomic Percentage**

T [K (°C)]	Elem.	Phase					
		Austenite	Ferrite	$\kappa$ -carbide	Pearlite		$M_{23}C_6$
					Ferrite	$\kappa$ -carbide	
<b>(a)</b>							
1073 (1050)	Fe	81.7	84.4				
	Mn	13.7	8.7				
	Al	4.6	6.9				
1023 (750)	Fe	81.3	86.1	69.6			
	Mn	14.8	7.9	21.4			
	Al	3.9	6.0	9.0			
973 (700)	Fe	80.3	86.9	68.1			
	Mn	15.0	7.0	23.0			
	Al	4.6	6.1	8.9			
948 (675)	Fe	81.2			87.0	65.5	
	Mn	14.1			7.1	24.5	
	Al	4.8			5.9	10.0	
923 (650)	Fe	82.4			89.0	66.2	
	Mn	14.0			6.4	24.7	
	Al	3.6			4.6	9.1	
898 (625)	Fe	81.5			89.0	65.4	55.0
	Mn	14.1			5.7	23.9	44.0
	Al	4.4			5.3	10.7	1.0
873 (600)	Fe				90.3	69.0	50.8
	Mn				5.3	23.1	48.2
	Al				4.4	7.9	1.0
848 (575)	Fe				88.9	57.0	56.6
	Mn				5.3	33.4	41.6
	Al				5.8	9.6	1.8
823 (550)	Fe				89.7	60.5	47.1
	Mn				4.4	31.2	51.8
	Al				5.9	8.3	1.1
773 (500)	Fe				90.4	59.3	
	Mn				4.6	31.6	
	Al				5.0	9.1	
<b>(b)</b>							
1073 (1050)	Fe	77.7	78.4				
	Mn	13.2	8.2				
	Al	9.1	13.4				
1023 (750)	Fe	77.8	80.6	63.3			
	Mn	14.4	7.7	19.8			
	Al	7.8	11.7	16.9			
973 (700)	Fe	76.3	81.6	61.9			
	Mn	14.6	6.7	22.2			
	Al	9.1	11.7	15.9			
948 (675)	Fe	77.1			81.8	59.0	
	Mn	13.6			6.8	22.4	
	Al	9.3			11.4	18.6	
923 (650)	Fe	79.2			84.8	60.1	
	Mn	13.7			6.2	22.8	
	Al	7.1			9.0	17.1	
898 (625)	Fe	77.7			84.3	58.5	53.9
	Mn	13.7			5.4	21.7	43.9
	Al	8.6			10.3	19.8	2.2
873 (600)	Fe				84.8	63.5	53.0
	Mn				4.9	21.7	43.9
	Al				10.3	14.8	3.1
848 (575)	Fe				83.6	51.4	55.1
	Mn				5.1	30.7	41.2
	Al				11.3	17.9	3.7

Table II. continued

T [K (°C)]	Elem.	Phase					
		Austenite	Ferrite	$\kappa$ -carbide	Pearlite		$M_{23}C_6$
					Ferrite	$\kappa$ -carbide	
823 (550)	Fe				84.3	55.3	46.1
	Mn				4.2	29.0	51.6
	Al				11.5	15.7	2.3
773 (500)	Fe				85.7	53.9	
	Mn				4.4	29.1	
	Al				9.9	17.0	

The error in Fe is about 0.25 pct, Mn 1.0 pct, and Al 10 pct.

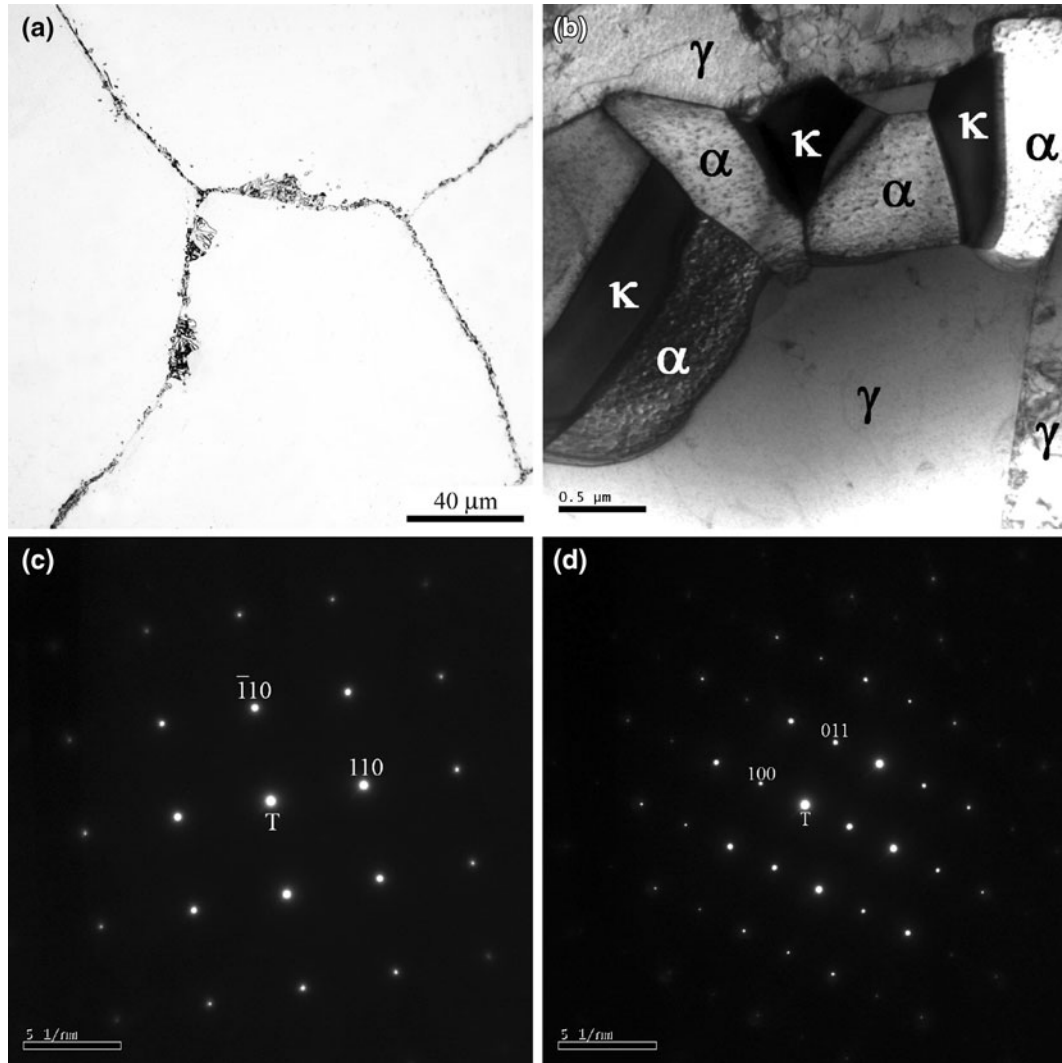


Fig. 5—(a) through (d) Further studies of the steel in OM and TEM after solution heat treatment at 1373 K and holding at a low temperature of 923 K for 100 h. (a) The OM showing the grain boundary precipitates. (b) A BF image shows that a lamellar colony develops at the austenite grain boundaries. The corresponding SAD patterns are from (c) [001] ferrite and (d) [011]  $\kappa$ -carbide in (b).

the constituent phases in wt pct and at. pct at various temperatures are also summarized in Table II(a) and (b), respectively. Note that Mn and Al concentrations of the  $\kappa$ -carbide are the highest among these three phases.

Study of the constituent phases of the Fe-C-Mn-Al alloy at lower temperatures was also carried out. Figure 5 shows the results of the OM and TEM investigations after isothermal holding of the steel at

923 K (650 °C). The OM in Figure 5(a) illustrates that the precipitates not only nucleated at the grain boundaries but also grew toward the austenite matrix as small nodules. The BF micrograph in Figure 5(b) reveals that a small nodule comprises lamellar ferrite and  $\kappa$ -carbide grains at the grain boundaries. Figure 5(c) shows the corresponding SAD pattern from the lamellar [001] ferrite and Figure 5(d) reveals that from lamellar [0 $\bar{1}$ 1]  $\kappa$ -carbide. This is direct evidence that an initial nodule of ferrite and  $\kappa$ -carbide develops from the austenite grain boundaries. Lamellae of ferrite and  $\kappa$ -carbide have also been investigated in ternary Fe-C-Al alloys<sup>[18]</sup> and quaternary Fe-C-Mn-Al alloys.<sup>[30,31]</sup> In the following context, we refer to the lamellae of ferrite and  $\kappa$ -carbide as  $\kappa$ -pearlite. From Table I, note that ferrite and  $\kappa$ -carbide co-precipitate at the austenite grain boundaries as separate grains at temperatures below 1023 K (750 °C), and as the  $\kappa$ -pearlite at temperatures below 948 K (675 °C). From Table II(a), the chemical compositions (wt pct) of the phases at 923 K (650 °C) are as follows: austenite matrix—Fe-14.0 Mn-3.6 Al; ferrite—Fe-6.4 Mn-4.6 Al; and  $\kappa$ -carbide—Fe-24.7 Mn-9.1 Al. Lamellar ferrite is high in Al and low in Mn, and lamellar  $\kappa$ -carbide is high in Mn and Al. Thus, the partitioning of Mn and Al is distinct in the lamellar ferrite and  $\kappa$ -carbide.

#### D. Austenite $\rightarrow$ Ferrite + $\kappa$ -Carbide + $M_{23}C_6$ Carbide

We discovered that a third phase of  $M_{23}C_6$  carbide is present in the  $\kappa$ -pearlite after the investigation of the lamellae of the steel at temperatures below 923 K (650 °C). As the OM shows in Figure 6, the  $\kappa$ -pearlite colonies in the austenite grew to large grain sizes after isothermal holding of the steel at 898 K (625 °C). Figure 7 shows the TEM analysis of the Fe-C-Mn-Al alloy which underwent the same isothermal holding condition as that of Figure 6. The TEM BF and dark-field (DF) images in Figures 7(a) and (b), respectively,

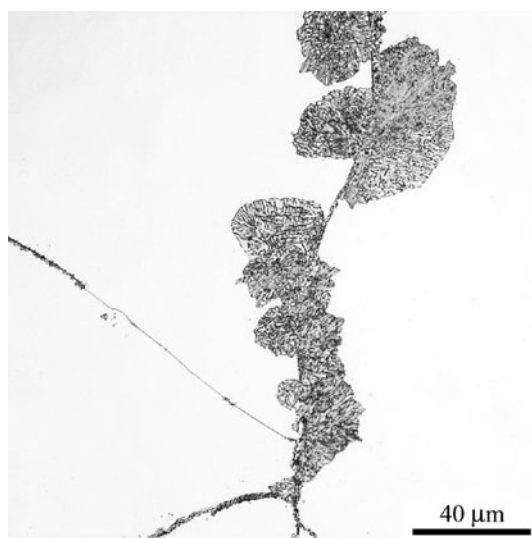


Fig. 6—The OM analysis of the steel after isothermal holding at 898 K for 100 h.

show a portion of the lamellar colony nucleating from the grain boundary and growing toward the upper-right austenite grain. Figures 7(c) and (d) shows the accompanying SAD patterns from the lamellar  $\alpha$  and  $\kappa$  grains, respectively. The zone-axis direction of the SAD pattern from the ferrite in Figure 7(c) is [0 $\bar{1}$ 1]. The SAD pattern in Figure 7(d) is from both [011]  $\kappa$ -carbide and [0 $\bar{1}$ 1] austenite on the upper-right side of Figure 7(a). The diffraction spots connected by white solid lines are from austenite. The Miller indices of the austenite phase in Figure 7(d) are also underlined to distinguish them from those of the  $\kappa$ -carbide. Note that the  $\kappa$ -carbide grew into the austenite matrix exhibiting a cube-on-cube orientation relationship (OR) with the austenite. The DF image in Figure 7(b) was taken using the reflections from both (011) planes of ferrite and (111) planes of austenite located at the lower-left-hand side, simultaneously, as they coexisted almost at the same diffraction spot, (011) <sub>$\alpha$</sub>  and (111) <sub>$\gamma$</sub> , in the SAD pattern shown in Figure 7(c). Thus, the DF image reveals the locations of the lamellar ferrite grains and the austenite grain on the lower-left side. After carefully identifying the different separate grains, we labeled them as  $\gamma$ ,  $\alpha$ , and  $\kappa$  on the BF and DF images in Figures 7(a) and (b). Therefore, direct evidence shows that lamellar ferrite and  $\kappa$ -carbide nucleate and grow side by side at the grain boundary and advance toward the austenite matrix as  $\kappa$ -pearlite colonies.

The identification of the  $M_{23}C_6$  carbide in the lamellae of the alloy at 898 K (625 °C) by TEM is revealed in Figure 8. The BF image in Figure 8(a) shows an interior area of a pearlite colony. The lamellae are composed of three different phases, of which one is the ferrite matrix ( $\alpha$ ), another consists of continuous long lamellar  $\kappa$ -carbide grains ( $\kappa$ ), and the third consists of small dark grains (C) located in the  $\alpha$  matrix or in contact with  $\kappa$ -carbide. Figure 8(b) is the accompanying SAD pattern taken from the thick lamellar  $\kappa$ -carbide plate at the center to top-left position and its neighboring ferrite matrix. The zone axes of the SAD pattern for the  $\kappa$ -carbide and ferrite in Figure 7(b) are along the [0 $\bar{1}$ 1] <sub>$\kappa$</sub>  and [ $\bar{1}$ 11] <sub>$\alpha$</sub>  directions, respectively. Note that an OR exists between the  $\kappa$ -carbide and ferrite, *i.e.*, [0 $\bar{1}$ 1] <sub>$\kappa$</sub> // [ $\bar{1}$ 11] <sub>$\alpha$</sub>  and (111) <sub>$\kappa$</sub> //(101) <sub>$\alpha$</sub> . This is the well-known Kurdjumov–Sachs (K–S) OR between FCC and BCC crystals. Figure 8(c) is the corresponding SAD pattern focusing on the small dark C grain in a center-right position, its neighboring ferrite matrix, and some of the  $\kappa$ -carbide grain. The SAD pattern in Figure 8(c) also covers the same reflections as those in Figure 8(b) from both ferrite and  $\kappa$ -carbide. Besides those from ferrite and  $\kappa$ -carbide, we observed several additional weak diffraction spots which are from the small C grain. After several more SAD patterns from the C grain were examined, the phase of the small dark C grain was confirmed to be  $M_{23}C_6$  carbide. The typical SAD patterns of  $M_{23}C_6$  carbide can be found in our previous articles.<sup>[14,15]</sup> The reflections of (111) planes of  $M_{23}C_6$  carbide are located at multiples of one-third positions between the ( $\bar{1}$ 10) ferrite reflections. In the SAD patterns shown in Figures 8(b) and (c), the strong reflections connected by thin solid white lines are from ferrite, and



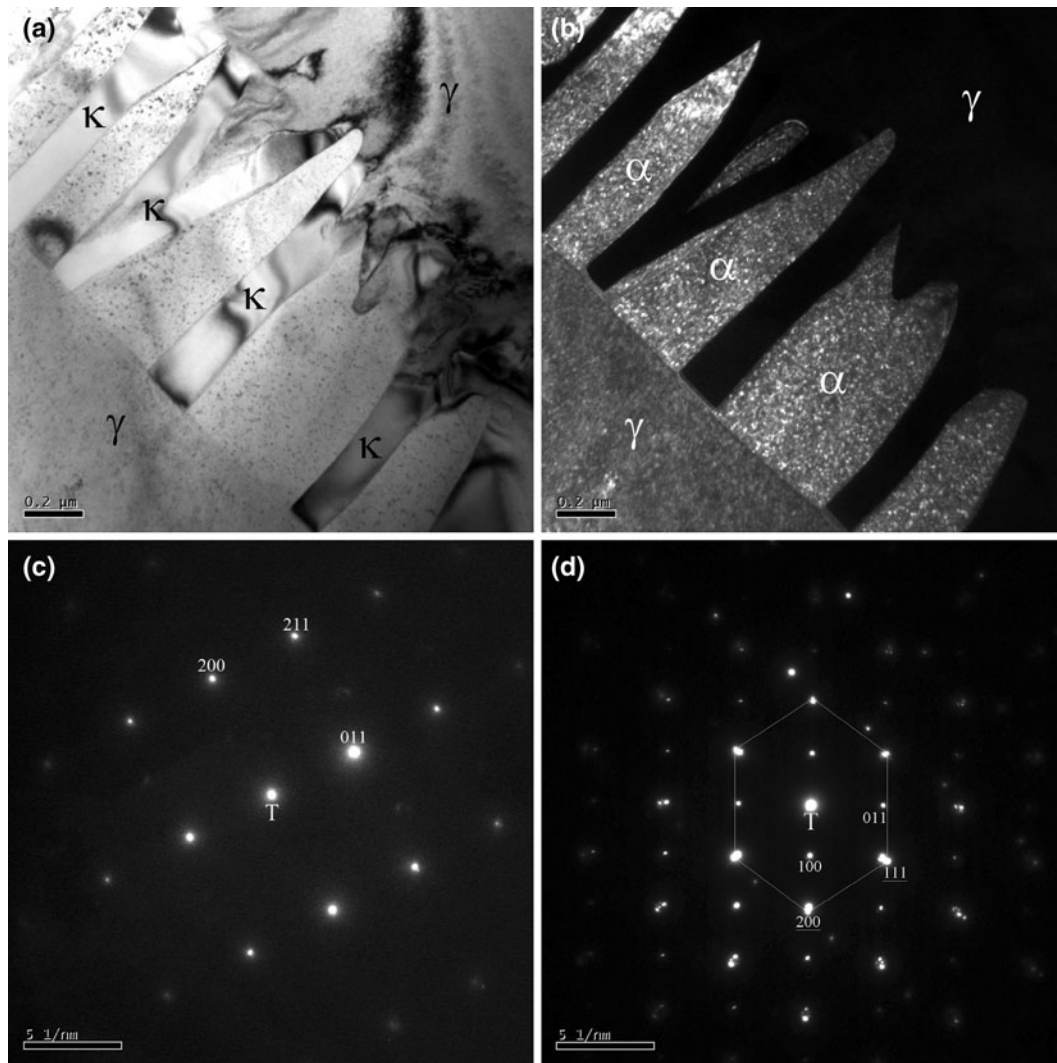


Fig. 7—A TEM analysis for the steel after 100-h isothermal holding at 898 K. (a) The BF image showing the initial stage of  $\kappa$ -pearlite. (b) The corresponding DF image to the BF image in (a) for  $(011)_\gamma$  and  $(111)_\gamma$  DF image of lamellar ferrite grains and austenite matrix at lower-left side. (c) The SAD pattern from the  $[0\bar{1}1]$  lamellar ferrite grain. (d) The SAD pattern from the  $[0\bar{1}1]$  lamellar  $\kappa$ -carbide and  $[0\bar{1}1]$  austenite at upper-right side. The diffraction spots connected by solid white lines are from austenite.

the plane Miller indices of ferrite are also underlined to distinguish them from those of  $\kappa$ -carbide and  $M_{23}C_6$  carbide. The strong reflections in the SAD patterns of Figures 8(b) and (c) are mostly from ferrite. The zone axes of the SAD pattern from the  $M_{23}C_6$ ,  $\kappa$ -carbide, and ferrite in Figure 8(c) are along the  $[0\bar{1}1]_C$ ,  $[0\bar{1}1]_\kappa$ , and  $[\bar{1}11]_\alpha$  directions, respectively. It is noteworthy that the K–S OR also exists between the  $M_{23}C_6$  carbide and ferrite, *i.e.*,  $[0\bar{1}1]_C//[\bar{1}11]_\alpha$  and  $(111)_C//(110)_\alpha$ . It shows that the closest packed direction,  $[0\bar{1}1]_C$ , of  $M_{23}C_6$  carbide is parallel to that of ferrite,  $[\bar{1}11]_\alpha$ , and the closest packed planes of  $M_{23}C_6$  carbide,  $(111)_C$ , are parallel to the close packed planes of ferrite,  $(110)_\alpha$ . The same K–S OR also exists between the lamellar  $M_{23}C_6$  carbide and ferrite in the  $M_{23}C_6$  pearlite of the Fe–C–Mn–Al alloys.<sup>[14,15]</sup> As the BF image shows in Figure 8(a), C stands for the  $M_{23}C_6$  carbide. So far, from the literature, only  $\kappa$ -pearlite with lamellae of (ferrite +  $\kappa$ -carbide)<sup>[30,31]</sup> and  $M_{23}C_6$  pearlite with

lamellae of (ferrite +  $M_{23}C_6$ )<sup>[14,15]</sup> were observed. No pearlite comprising lamellae of ferrite,  $\kappa$ -carbide, and  $M_{23}C_6$  carbide has been previously reported. Therefore, we present here the first observation of  $M_{23}C_6$  carbide in the  $\kappa$ -pearlite.

The compositions (wt pct) of the constituent phases of the alloy at 898 K (625 °C) as indicated in Table II(a) as follows: austenite—Fe-14.2 Mn-4.4 Al; ferrite—Fe-5.7 Mn-5.3 Al;  $\kappa$ -carbide—Fe-23.9 Mn-10.7 Al; and  $M_{23}C_6$  carbide—Fe-44.0 Mn-1.0 Al. Note that Mn occupies almost half of the metallic portion of the  $M_{23}C_6$  carbide. The composition of  $M_{23}C_6$  carbide is high in Mn and low in Al. It is noteworthy that the manganese content of the constituent phases of the steel in descending order is  $M_{23}C_6$ ,  $\kappa$ -carbide, austenite, and ferrite. The Al content of the phases in decreasing order is  $\kappa$ -carbide, ferrite, austenite, and  $M_{23}C_6$  carbide. The low Al content of  $M_{23}C_6$  carbide in Fe–C–Al alloys was discovered by Frommeyer *et al.*<sup>[18]</sup> and in Fe–C–Mn–Al alloys

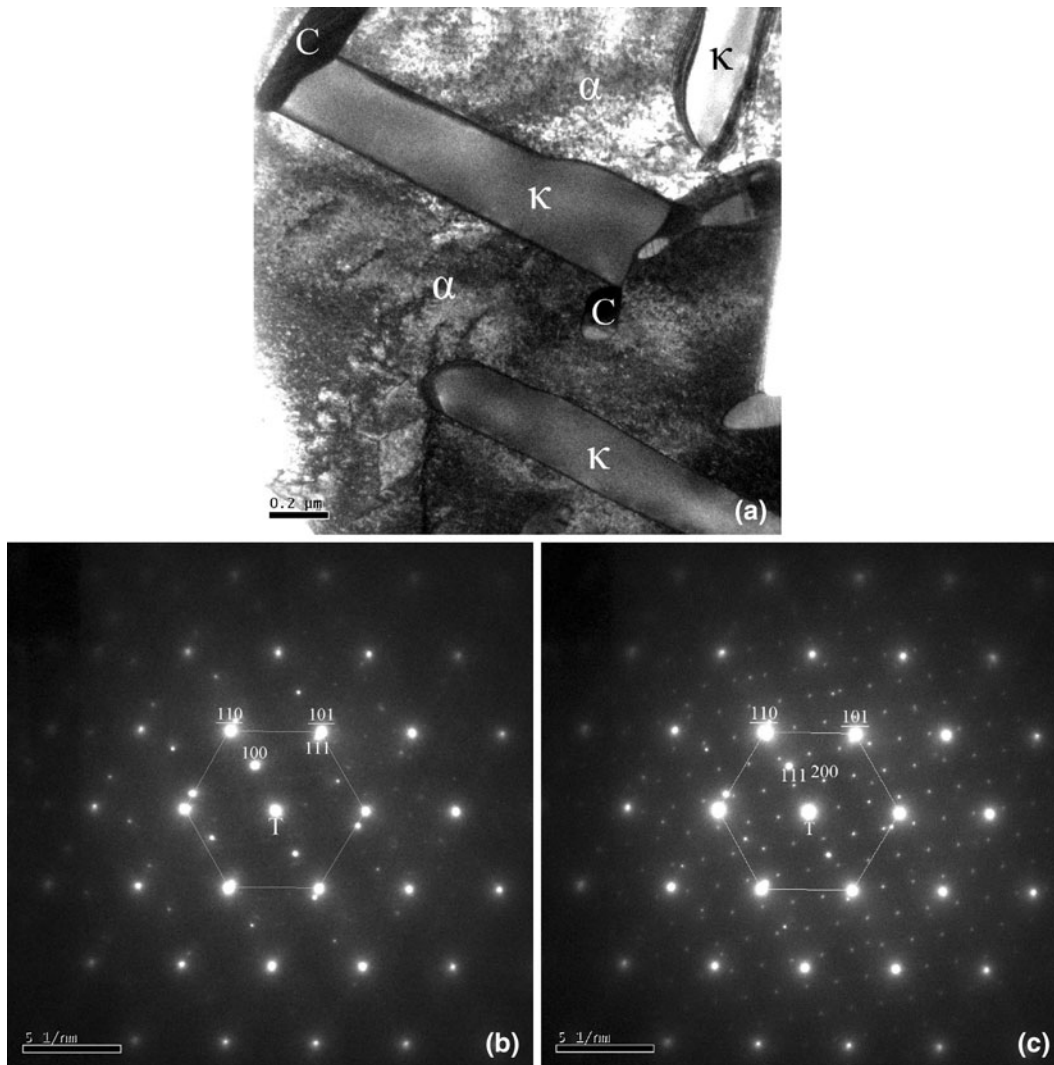


Fig. 8—Another TEM analysis of the steel after isothermal holding at 898 K. (a) The BF image showing a portion of the  $\kappa$ -pearlite which indicates the distribution of  $\kappa$  and  $M_{23}C_6$  carbides in the ferrite grain of the  $\kappa$ -pearlite. (C:  $M_{23}C_6$  carbide). (b) The SAD patterns from the  $[0\bar{1}1]$   $\kappa$ -carbide and  $[\bar{1}11]$  ferrite grains. (c) The SAD patterns covering the  $[0\bar{1}1]$   $M_{23}C_6$  carbide,  $[0\bar{1}1]$   $\kappa$ -carbide, and  $[\bar{1}11]$  ferrite grains. The strong reflections of ferrite are connected by thin solid white lines, and the plane Miller indices of ferrite are also underlined to distinguish them from those of  $\kappa$ -carbide and  $M_{23}C_6$  carbide.

by Cheng *et al.*<sup>[14,15]</sup> Therefore, the partitioning of Mn and Al is also evident in the lamellae of ferrite,  $\kappa$ -carbide, and  $M_{23}C_6$  carbide. The precipitation of different carbides in the austenite, as alloy partition proceeds, is a well-known phenomenon in alloy steels, for example, MC carbide precipitates in the  $M_3C$  pearlite of Fe-C-V alloys.<sup>[40]</sup>

When  $\kappa$ -pearlite was first discovered, lamellae of ferrite and  $\kappa$ -carbide were assumed to be the product phases of a eutectoid reaction which was proposed in such steels as the Fe-C-Al<sup>[18]</sup> and Fe-C-Mn-Al alloys.<sup>[30]</sup> The partitioning of the Mn solute in ferrite and  $\kappa$ -carbide could be the result of the redistribution of the solutes in the original austenite after the austenite decomposed. It could be a eutectoid reaction. However, it is not reasonable to expect that the Al contents of both second phases are higher than that of the parent austenite. Were it a eutectoid reaction, in which unstable austenite would decompose into ferrite and  $\kappa$ -carbide,

the Al content of the austenite should be at an intermediate level between those of the two product phases. The observations do not satisfy the condition of mass balance. Thus, ferrite and  $\kappa$ -carbide form from the less frequently observed reaction. Further study of the constituent phases at low temperatures did not clearly reveal the type of phase transformation which precedes the appearance of  $M_{23}C_6$  carbide in the  $\kappa$ -pearlite lamellae.  $M_{23}C_6$  carbide contains a low Al concentration. The condition of mass balance is satisfied when the  $M_{23}C_6$  carbide is joined to the lamellae of ferrite and kappa-carbide. Therefore, we must recognize that these three phases are product phases of a eutectoid reaction. The eutectoid reaction of the quaternary Fe-C-Mn-Al alloy at constant pressure is a univariant reaction, not an invariant reaction. The eutectoid compositions of the constituent phases may vary with the temperature. Since the Al concentration of the steel is higher than the eutectoid Al concentration, ferrite and  $\kappa$ -carbide appear

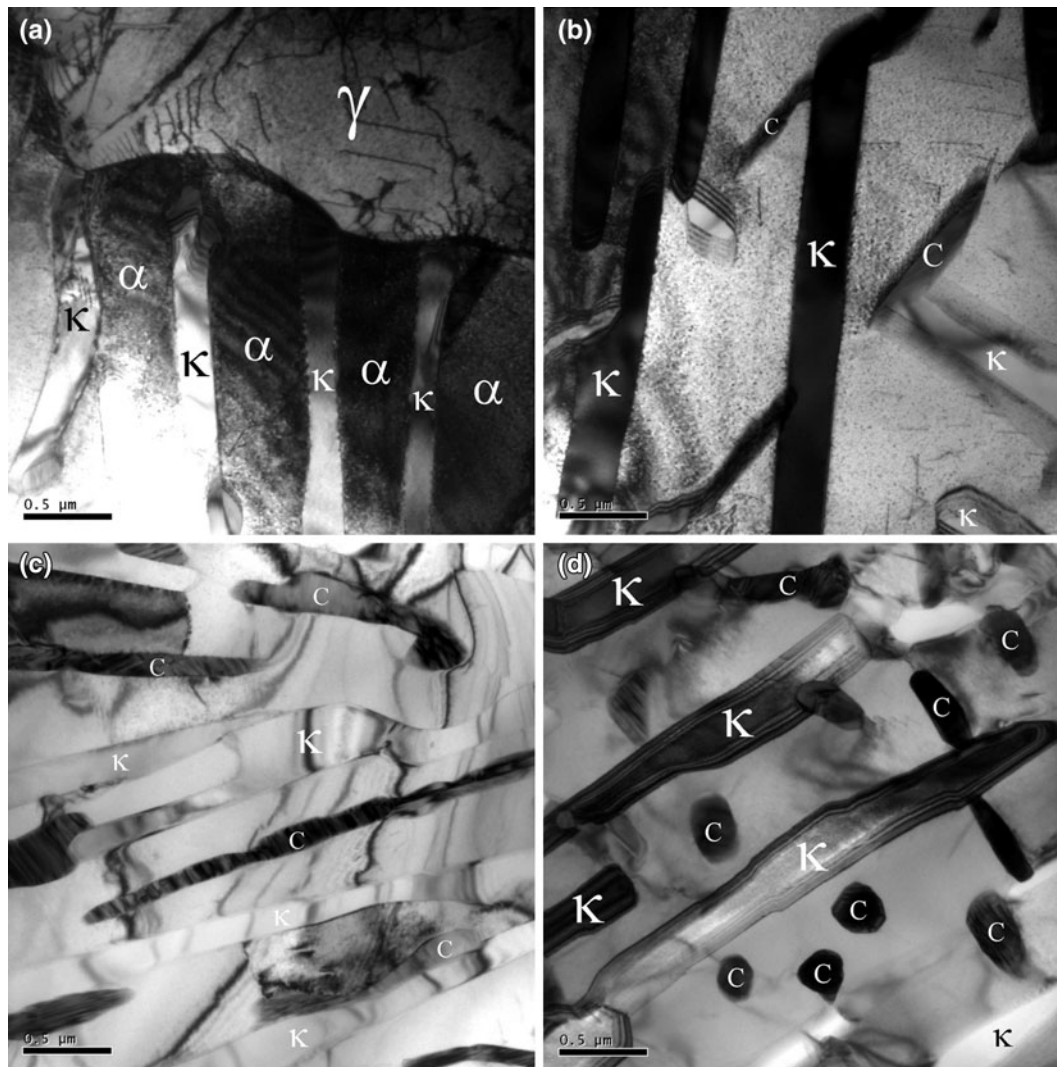


Fig. 9—(a) through (d) BF images of the Fe-C-Mn-Al alloy after the isothermal holding at 898 K.

prior to the eutectoid reaction to reduce the Al content of the residual austenite. Thus, the second phases of ferrite and  $\kappa$ -carbide existing in the austenite at temperatures above the eutectoid temperature are proeutectoid phases. The occurrence of proeutectoid phases is attributed to the fact that the original Al content of the austenite is higher than the eutectoid Al concentration of the steel. Proeutectoid ferrite and  $\kappa$ -carbide appear at the grain boundaries at temperatures below 1073 K (800 °C). Separate grains of ferrite and  $\kappa$ -carbide exist in the steel at temperatures of 1073 K and 973 K (800 °C and 700 °C). Lamellar colonies of ferrite and  $\kappa$ -carbide form at temperatures below 973 K (700 °C) as  $\kappa$ -pearlite. Upon isothermal holding of the Fe-C-Mn-Al alloy below the eutectoid temperature, for example, at 898 K (625 °C), proeutectoid ferrite and  $\kappa$ -carbide appear as  $\kappa$ -pearlite at the initial stage to reduce the Al content of the residual austenite. After the proeutectoid phases of ferrite and  $\kappa$ -pearlite develop to a certain volume fraction,  $M_{23}C_6$  carbide appears in the lamellae of ferrite,  $\kappa$ -carbide, as the result of the decomposition of the retained austenite. Therefore, the overall phase

transformation of the Fe-C-Mn-Al alloy at temperatures below 923 K (650 °C) is the eutectoid reaction, *i.e.*, austenite  $\rightarrow$  ferrite +  $\kappa$ -carbide +  $M_{23}C_6$  carbide.

Several different morphologies of  $M_{23}C_6$  carbide in the  $\kappa$ -pearlite were discovered. Here, some features of the  $M_{23}C_6$  precipitates are reported. Different colonies of the  $\kappa$ -pearlite are revealed in the BF images shown in Figure 9. The Fe-C-Mn-Al alloy in Figure 9 underwent isothermal holding at 898 K (625 °C). The BF image in Figure 9(a) shows the edge of a  $\kappa$ -pearlite colony in the austenite matrix. Straight lamellar  $\kappa$ -carbide plates are present along with lamellar ferrite grains in which no  $M_{23}C_6$  carbide grains have precipitated. However, this is not always the case when examining the edges of the  $\kappa$ -pearlite colonies. Some ferrite grains of the  $\kappa$ -pearlite colonies have  $M_{23}C_6$  precipitates. The BF images in Figures 9(b) through (d) illustrate the internal sections of various  $\kappa$ -pearlite colonies. Figure 9(b) reveals some straight lamellar  $\kappa$ -carbide plates, almost perpendicular in the BF image. Smaller lamellar  $M_{23}C_6$  carbide grains touch  $\kappa$ -carbide plates at approximately 45 degrees and cross the ferrite matrix. Figure 9(c) shows several

near-horizontal  $\kappa$ -carbide plates in the ferrite matrix. Thin lamellar  $M_{23}C_6$  carbide grains appear in the ferrite matrix and are nearly parallel to the  $\kappa$ -carbide plates. The lamellar  $M_{23}C_6$  grain in the central area is irregularly thin and long. Note that a thin lamellar grain of  $M_{23}C_6$  carbide even adheres to the  $\kappa$ -carbide plate on the lower-right side of the BF image in Figure 9(c). A different feature of  $M_{23}C_6$  carbide in the lamellae is illustrated in Figure 9(d). Here, some of the  $M_{23}C_6$  carbide precipitates are in the form of small grains and are located in the ferrite between two separate lamellar  $\kappa$ -carbide grains. Other  $M_{23}C_6$  carbide grains are in the form of lamellar grains connected between two  $\kappa$ -carbide plates. Therefore, the BF images in Figure 9 reveal that the  $M_{23}C_6$  carbide precipitates can adopt a range of morphologies in the  $\kappa$ -pearlite. Thus far, no separate lamellae of ferrite and  $M_{23}C_6$  carbide without surrounding lamellar  $\kappa$ -carbide grains have been observed in TEM. All the  $M_{23}C_6$  carbide grains appear in the  $\kappa$ -pearlite. Thus, the  $M_{23}C_6$  carbide is precipitated

in the ferrite matrix of the  $\kappa$ -pearlite. We investigated several TEM samples and found that at the beginning of the formation of pearlite colonies, no  $M_{23}C_6$  carbide precipitates are present in the lamellar ferrite grains of the lamellae, as shown in Figure 7. When the volume fraction of the lamellar colonies increases above a certain critical value, the  $M_{23}C_6$  carbide grains begin to precipitate in the lamellae. It is noteworthy that in the BF observation of Figure 9(a), it is difficult to determine whether the  $\kappa$ -pearlite is located at the grain boundary or not. If it is, this might also indicate the initial growth stage of proeutectoid  $\kappa$ -pearlite.

From the above observations, we determine the upper temperature limit of the eutectoid reaction to produce lamellae of ferrite,  $\kappa$ -carbide, and  $M_{23}C_6$  carbide as lying between 923 K and 898 K (650 °C and 625 °C). Though we did not acquire sufficient data to obtain the complete TTT diagram for the eutectoid reaction, it is still possible to determine the temperature of the nose region of the TTT curve by isothermal holding of the

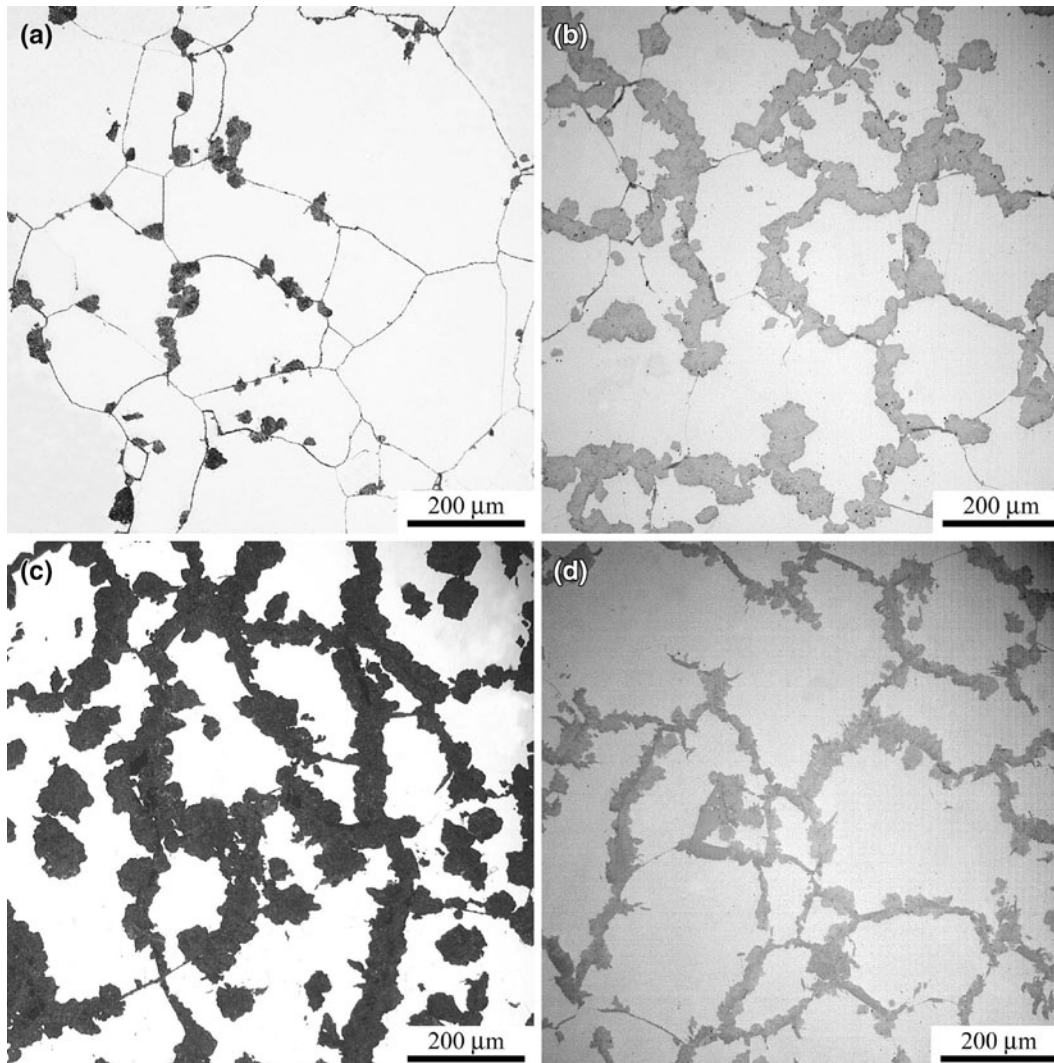


Fig. 10—The OMs of the steel after solution heat treatment at 1373 K and holding at different low temperatures for 100 h. The temperatures are indicated as follows: (a) 898 K, (b) 873 K, (c) 848 K, and (d) 823 K.

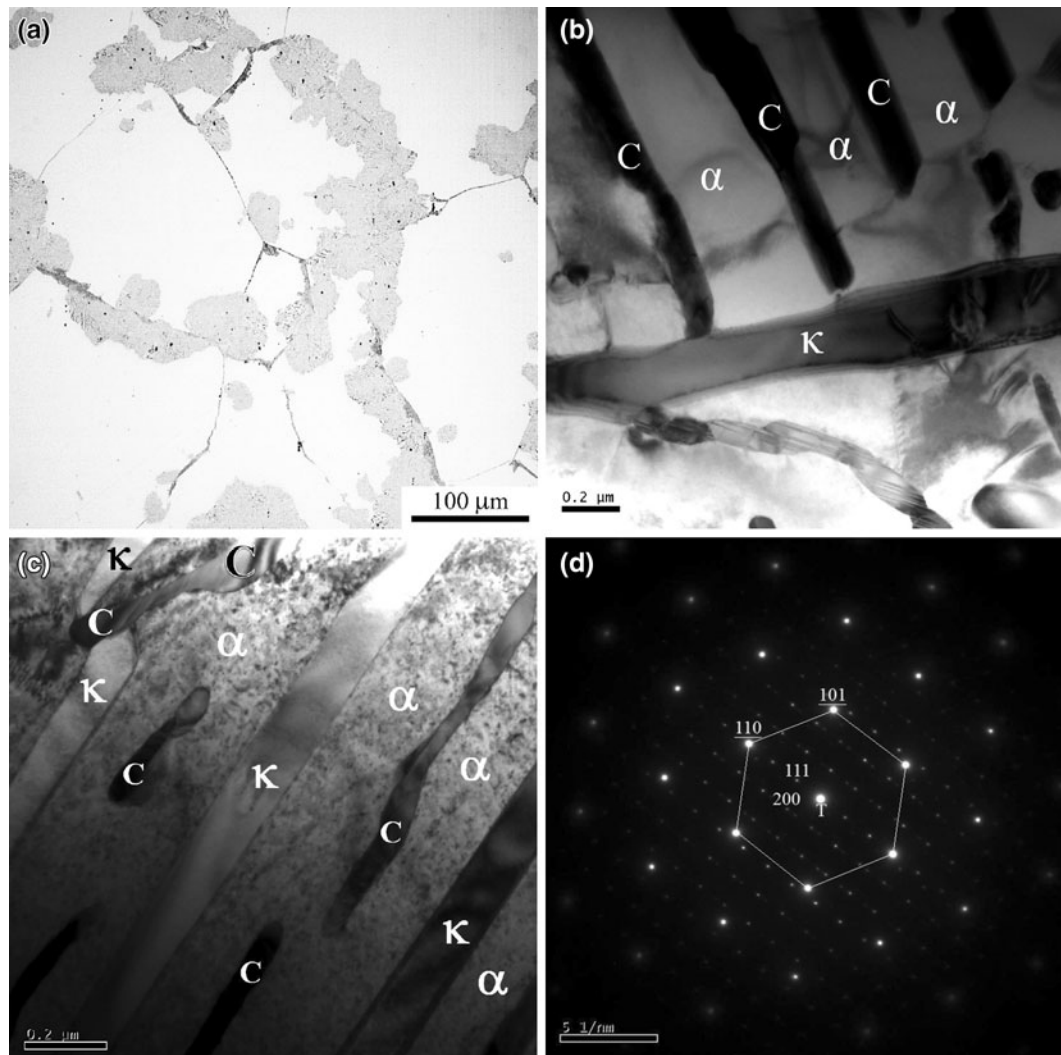


Fig. 11—(a) The OM showing large  $\kappa$ -pearlite colonies in the austenite. (b) and (c) The BF images revealing the internal portions of various  $\kappa$ -pearlites. (d) The SAD pattern taken at  $[0\bar{1}1]_{M_{23}C_6}$  carbide and  $[\bar{1}11]_{\text{ferrite}}$  matrix in (c). The heat treatment of the alloy was the solution heat treatment at 1373 K and 100-h isothermal holding at 873 K.

steel at various low temperatures, while maintaining the same holding time interval of 100 hours, by means of the OMs shown in Figure 10. The temperatures for the isothermal holding process in Figures 10(a) through (d) are (a) 898 K (625 °C), (b) 873 K (600 °C), (c) 848 K (575 °C), and (d) 823 K (550 °C). The figure shows that the volume fraction of the  $\kappa$ -pearlite is the highest at 848 K (575 °C) (Figure 10(c)). Therefore, we conclude that the nose temperature of the TTT curve for the appearance of the pearlite phases in the Fe-C-Mn-Al alloy is close to 848 K (575 °C).

Various  $M_{23}C_6$  grains in the ferrite matrix of  $\kappa$ -pearlite have been investigated at temperatures below 898 K (625 °C). Figure 11 shows the OM and TEM analyses for the alloy after 100-hour isothermal holding at 873 K (600 °C). As the OM shows in Figure 11(a), the  $\kappa$ -pearlite colonies occupy a greater volume fraction in the austenite than those of the alloy treated at 898 K (625 °C), as shown in Figure 6. The BF images in Figures 11(b) and (c) show the internal parts of two different pearlite colonies. The lamellae are composed of

the ferrite matrix, continuous long and thick  $\kappa$ -carbide plates, and a thin layer or small grains of  $M_{23}C_6$  carbide. Figure 11(d) is the corresponding SAD pattern taken from the thin lamellar  $M_{23}C_6$  carbide and its neighboring ferrite matrix in Figure 11(c). The zone axes of the SAD pattern from the  $M_{23}C_6$  carbide and ferrite are along the  $[0\bar{1}1]_C$  and  $[\bar{1}11]_z$  directions, respectively. The same K-S OR, mentioned before, exists between the FCC  $M_{23}C_6$  carbide and BCC ferrite, *i.e.*,  $[0\bar{1}1]_C // [\bar{1}11]_z$  and  $(111)_C // (101)_z$ .

A series of secondary electron images (SEIs) from the SEM are shown in Figure 12 after the steel has undergone 100-hour isothermal holding at 873 K (600 °C). The SEI in Figure 12(a) is at the lowest magnification and the field shown covers all other SEIs in Figures 12(b) through (f). Figures 12(b), (c), and (d) represents one series of SEIs of a given region of Figure 12(a) at increasing magnifications, and Figures 12(e) and (f) shows another part of Figure 12(a) at increasing magnification. The compositions of the constituent phases shown in the SEIs have also been

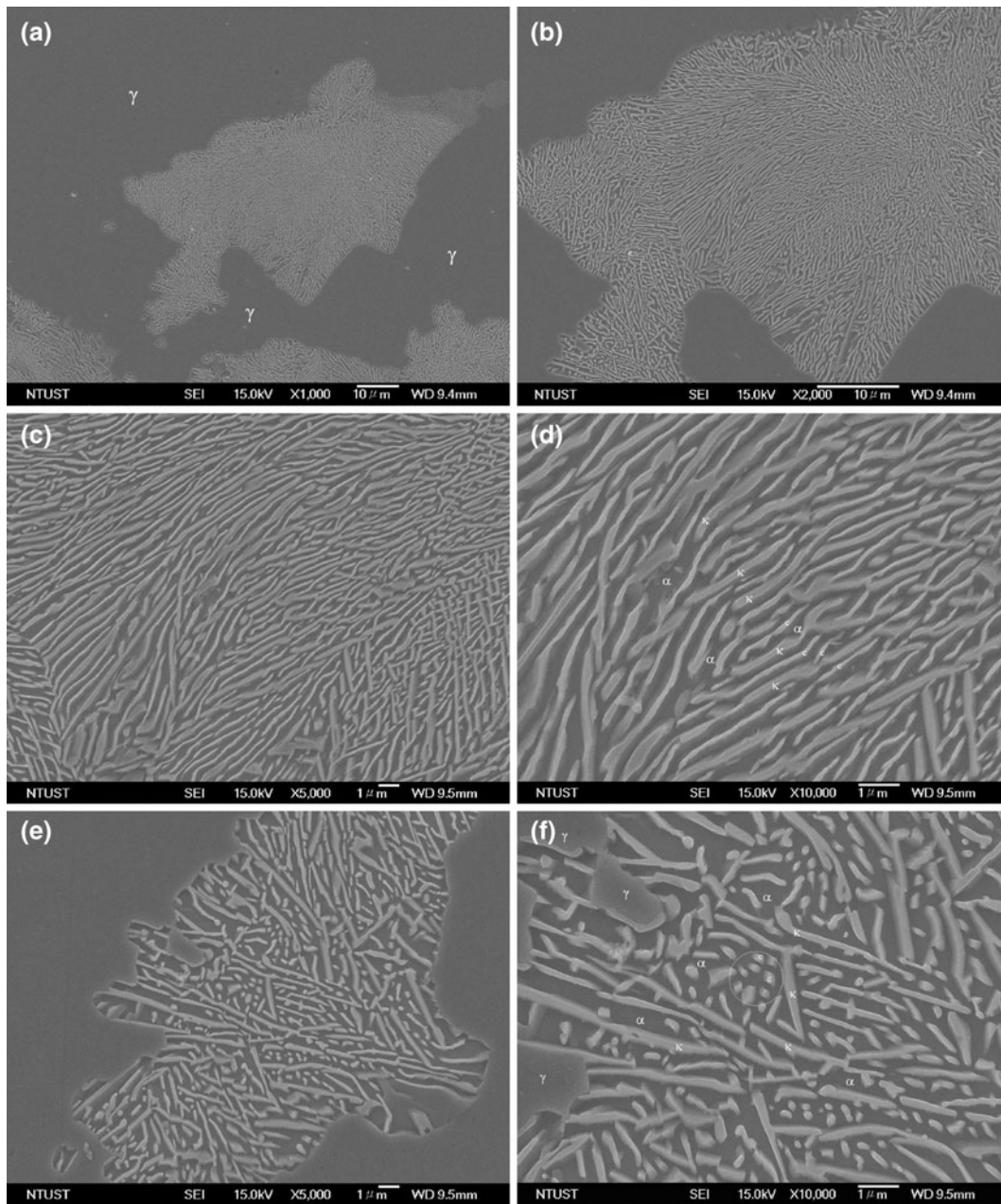


Fig. 12—(a) through (f) SEIs, with different magnifications from the SEM for the steel after isothermal holding at 873 K for 100 h. (a) is at the lowest magnification and the field shown covers all other SEIs in (b) to (f). (b), (c), and (d) represent one series of SEIs of a given region in (a) at increasing magnifications. (e) and (f) show another part in (a) at increasing magnifications. In (d) and (f), thin irregular lamellar and isolated small grains of  $M_{23}C_6$  carbide are between thick lamellar layers of  $\kappa$ -carbide ( $\gamma$ : austenite;  $\alpha$ : ferrite;  $\kappa$ :  $\kappa$ -carbide; and C:  $M_{23}C_6$  carbide).

measured by the EDS (which is a standard accessory of the SEM). Thus, it is not difficult to determine the constituent phases in the SEI from the compositions, morphologies, and relative locations of the phases in the austenite. In Figures 12(d) and (f), we marked the constituent phases distributed in the  $\kappa$ -pearlite for easy comparison, for example,  $\alpha$  for ferrite matrix,  $\kappa$  for  $\kappa$ -carbide, and C for  $M_{23}C_6$  carbide. Austenite is also marked as  $\gamma$  as the OM in Figure 12(f) covers some portions of the austenite matrix. The  $\kappa$ -pearlite consisting of ferrite,  $\kappa$ -carbide, and  $M_{23}C_6$  carbide developed in the austenite. In the  $\kappa$ -pearlite, ferrite is the matrix, thick

$\kappa$ -carbide plates run through the matrix, and small plates or grains of  $M_{23}C_6$  carbide are distributed between the  $\kappa$ -carbide plates. After the determination of the phases in SEIs, it was found that the relative heights of the constituent phases from the highest to lowest in the SEI are as follows:  $M_{23}C_6$  carbide,  $\kappa$ -carbide, austenite, and ferrite.

Lamellae of ferrite and  $\kappa$ -carbide in the proeutectoid and eutectoid reactions are lamellar pearlite.<sup>[9]</sup> However, the  $M_{23}C_6$  carbide precipitating in the  $\kappa$ -pearlite is, somehow, not always lamellar. Judging from various micrographs in the SEM and TEM studies of the  $M_{23}C_6$

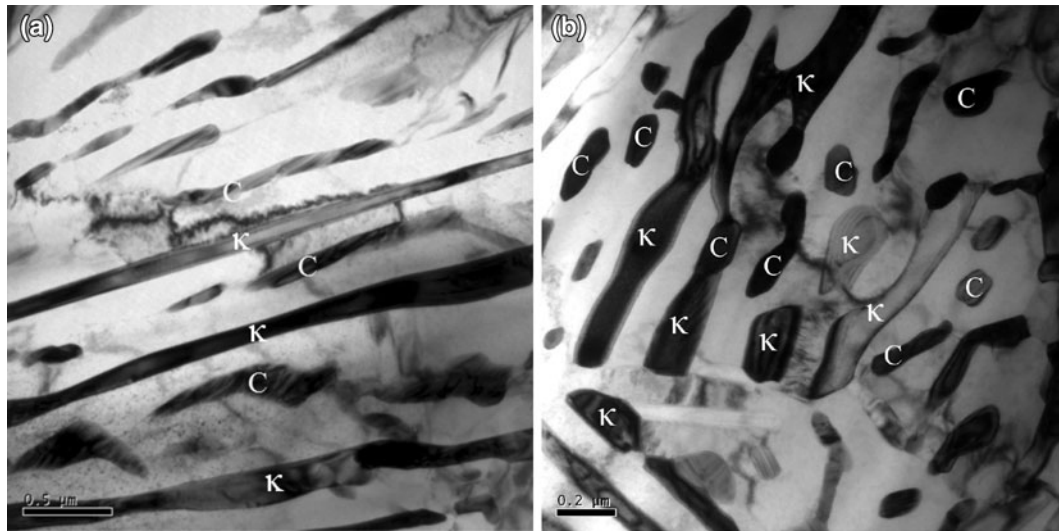


Fig. 13—TEM BF observation of the steel after isothermal holding at (a) 848 K and (b) 823 K for 100 h.

carbide, we might think of the shape of  $M_{23}C_6$  carbide in the lamellae as thin, long rods, not lamellar plates similar to  $\kappa$ -carbide. Thus, if viewing the  $M_{23}C_6$  carbide in different directions, it can occur in the form of thin, long (lamellar) grains, such as those shown in Figures 9(c), 11(a), and 12(d), and in the form of small (non-lamellar) grains, such as those in Figures 9(d) and 12(f).<sup>[9]</sup> When long, thick lamellar  $\kappa$ -carbide grains, along with ferrite, move forward into the austenite matrix,  $M_{23}C_6$  carbide may or may not precipitate inside the ferrite matrix. Ferrite may occur with  $M_{23}C_6$  carbide grains in the lamellae. Some thin  $M_{23}C_6$  layers in the ferrite may be nearly parallel to the thick  $\kappa$ -carbide plates. They may be connected between two parallel  $\kappa$ -carbide plates. Thin lamellar  $M_{23}C_6$  carbide grains may contact the  $\kappa$ -carbide plates at one end and cross the ferrite matrix at the other end. Some small separate  $M_{23}C_6$  grains may be located in the ferrite matrix between lamellar grains of  $\kappa$ -carbide. Thus, most thin lamellar grains and small grains distributed in the ferrite matrix between thick  $\kappa$ -carbide plates are  $M_{23}C_6$  carbide grains. We have seen clusters of  $M_{23}C_6$  carbide in the ferrite matrix, which closely resemble  $M_{23}C_6$  pearlite in Fe-C-Mn-Al alloys.<sup>[14,15]</sup> However, in the SEM study, it is quite clearly shown that  $M_{23}C_6$  grains in the ferrite matrix are surrounded by long  $\kappa$ -carbide plates, for example, in the center circled area in Figure 13(f), and thus, it is not a  $M_{23}C_6$  pearlite, but a part of the  $\kappa$ -pearlite.

The study of the  $\kappa$ -pearlite colonies at temperatures below 873 K is shown in Figure 13. Figure 13(a) and (b) illustrates a TEM study of the steel after 100-hour isothermal holding at 848 K and 823 K (575 °C and 550 °C), respectively. The BF image in Figure 13(a) shows the internal section of the  $\kappa$ -pearlite of the steel at 848 K. The matrix phase of the lamellae is ferrite, long and thick lamellar grains are  $\kappa$ -carbide, and  $M_{23}C_6$  carbide grains are in the form of small lamellar grains located between  $\kappa$ -carbide plates. Figure 13(b) shows a

BF micrograph of the  $\kappa$ -pearlite at 823 K (550 °C). The  $M_{23}C_6$  carbide grains are in the form of small separate grains between  $\kappa$ -carbide plates which are located in the ferrite matrix. Note that the size of the second phases becomes smaller than those produced at higher temperatures, for example, at 898 K (625 °C) as shown in Figure 9. Thus, the eutectoid product phases of ferrite,  $\kappa$ -carbide, and  $M_{23}C_6$  carbide appear in the austenite matrix at temperatures of 848 K and 823 K (575 °C and 550 °C). When we investigated the constituent phases of the  $\kappa$ -pearlite for the steel isothermally held at 773 K (500 °C) for 100 hours, only lamellae of ferrite and  $\kappa$ -carbide were discovered. No  $M_{23}C_6$  carbide was found. The lack of  $M_{23}C_6$  carbide in the ferrite matrix of the  $\kappa$ -pearlite might be due to the short isothermal holding time.

All the constituent phases at various temperatures are summarized in Table I. The compositions of the constituent phases at different temperatures are also summarized in Tables II(a) and (b). According to Table II(b), we plotted the variations of the Fe, Mn, and Al compositions of the constituent phases with temperature in Figure 14. The metallic compositions (at. pct) of ferrite,  $\kappa$ -carbide, and  $M_{23}C_6$  carbide are revealed in Figures 14(a), (b), and (c), respectively. From Table II and Figure 14, we can see that the Mn content in ferrite and  $\kappa$ -carbide varies with the temperature. Upon decreasing the temperature, the Mn content of ferrite decreases, while that of  $\kappa$ -carbide increases. The Al contents of all the constituent phases were not affected by temperature change. The variation of the metallic compositions of the austenite and  $M_{23}C_6$  carbide with temperature is uncertain. Thus, it is somewhat difficult to determine the eutectoid trough by tracing the concentration variation of the austenite with decreasing temperature.

Before discussing the possible growth mechanism of the eutectoid phases, we must recognize that the nominal carbon concentrations of the constituent phases, in descending order, are  $M_{23}C_6$  carbide,

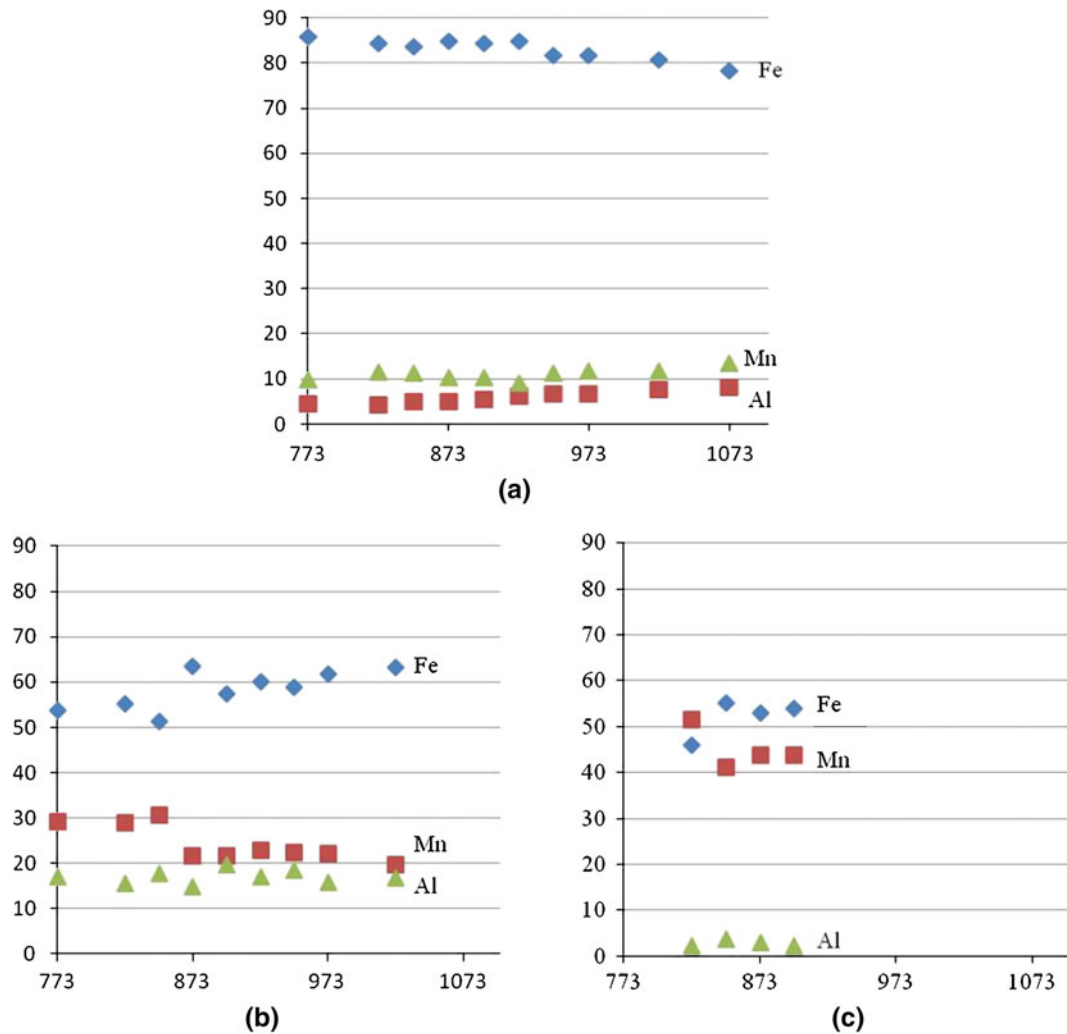


Fig. 14—According to Table II(b), the variations of the metallic compositions (at. pct) with temperatures (K) in the constituent phases of the alloy: (a) ferrite, (b)  $\kappa$ -carbide, and (c)  $M_{23}C_6$  carbide.

$\kappa$ -carbide, austenite, and ferrite. During the growth of the proeutectoid  $\kappa$ -pearlite in the austenite, prior to the eutectoid reaction, lamellar ferrite and  $\kappa$ -carbide may grow cooperatively. Ferrite grows to consume the Al atoms from the austenite and to expel excess Mn and C solutes to the austenite. Thus, areas adjacent to the ferrite grains are suitable for the growth of  $\kappa$ -carbide grains with a high Mn and C concentration. During the  $\kappa$ -carbide growth, Al, Mn, and C atoms are depleted from the neighboring austenite regions. Areas low in Mn and C solutes are favored sites for the growth of ferrite. However, both ferrite and  $\kappa$ -carbide have higher Al concentrations than the austenite. For the conservation of the solute atoms, a net flux of Al atoms must be supplied from the austenite matrix away from the reaction front. Thus, Al atoms migrate from the distant austenite matrix to the growing edge of the lamellar ferrite and  $\kappa$ -carbide. This causes low Al content of the residual austenite, the composition of which may be close to the eutectoid composition. After the growth of the proeutectoid  $\kappa$ -pearlite, the composition of the

residual austenite approaches the eutectoid composition. Retained austenite decomposes into ferrite,  $\kappa$ -carbide, and  $M_{23}C_6$  carbide following the eutectoid reaction. Therefore, the average concentration of the final product phases must be equal to that of the retained austenite as the result of the eutectoid reaction.

In accordance with the calculated phase diagrams in Figure 2, the constituent phases of the Fe-C-Mn-Al alloy upon cooling from 1073 K are as follows: austenite  $\rightarrow$  austenite + ferrite  $\rightarrow$  austenite + ferrite +  $\kappa$ -carbide  $\rightarrow$  austenite + ferrite +  $\kappa$ -carbide +  $M_7C_3$  carbide  $\rightarrow$  ferrite +  $\kappa$ -carbide +  $M_{23}C_6$  carbide. However, according to Table I, the experimentally determined phases of the Fe-C-Mn-Al alloy upon decreasing the isothermal holding temperature below 1023 K (750 °C) are as follows: austenite  $\rightarrow$  austenite + ferrite  $\rightarrow$  austenite + ferrite +  $\kappa$ -carbide  $\rightarrow$  austenite + ferrite +  $\kappa$ -carbide +  $M_{23}C_6$  carbide. When the experimentally determined phases shown in Table I are compared with those theoretically calculated in Figure 2, the most significant difference is that no  $M_7C_3$  carbide was found



experimentally. Otherwise, the temperatures for the appearance of ferrite and (ferrite +  $\kappa$ -carbide) in the austenite matrix are quite similar, although approximately 30 K lower for the theoretical calculation. However, the temperature for the appearance of the  $M_{23}C_6$  carbide is much lower in the calculated phase diagram. It is worth noting that even in the calculated phase diagram in Figure 2(e), there are sudden jumps in the proportions of ferrite,  $\kappa$ -carbide, and  $M_{23}C_6$  carbide because of the disappearance of the retained austenite, and this might be the evidence of the eutectoid reaction: austenite  $\rightarrow$  ferrite +  $\kappa$ -carbide +  $M_{23}C_6$  carbide. Therefore, the theoretical prediction of the eutectoid reaction is coincidentally matched with experimental observation.

#### IV. CONCLUSIONS

The eutectoid reaction in a quaternary Fe-C-Mn-Al alloy has been investigated at a composition of Fe-13.5 Mn-6.3 Al-0.78 C (wt pct). The upper temperature limit for the eutectoid reaction lies between 923 K and 898 K (650 °C and 625 °C). Lamellae of ferrite,  $\kappa$ -carbide, and  $M_{23}C_6$  carbide are involved in the eutectoid reaction after the retained austenite decomposes as follows: austenite  $\rightarrow$  ferrite +  $\kappa$ -carbide +  $M_{23}C_6$  carbide. As the Al content of the steel is higher than that of the eutectoid composition, ferrite and  $\kappa$ -carbide, which contain higher Al contents than the austenite, appear in the austenite prior to the eutectoid reaction. Therefore, ferrite and  $\kappa$ -carbide initially play roles as proeutectoid phases to reduce the Al content of the retained austenite, which decomposes into ferrite,  $\kappa$ -carbide, and  $M_{23}C_6$  carbide during the eutectoid reaction at a later stage. Proeutectoid ferrite and  $\kappa$ -carbide appear at the grain boundaries at temperatures below 1073 K (800 °C). Separate grains of ferrite and  $\kappa$ -carbide exist in the steel at temperatures between 1073 K and 973 K (800 °C and 700 °C). Lamellar colonies of ferrite and  $\kappa$ -carbide form at temperatures below 973 K (700 °C) as  $\kappa$ -pearlite. During isothermal holding at temperatures below the eutectoid temperature, lamellae of ferrite and  $\kappa$ -carbide, *i.e.*, the proeutectoid phases, develop at the grain boundaries prior to the eutectoid reaction, and  $M_{23}C_6$  carbide appears in the ferrite matrix as either irregular thin lamellar grains or small isolated grains in the lamellae after the proeutectoid  $\kappa$ -pearlite colonies grow above a certain volume fraction. Therefore,  $M_{23}C_6$  carbide,  $\kappa$ -carbide, and ferrite are product phases from the eutectoid reaction.

#### ACKNOWLEDGMENTS

The authors at the National Taiwan University of Science and Technology acknowledge the financial support for this article by the National Science Council, Taiwan, under Grant No. NSC-102-2221-E-011-022.

#### REFERENCES

1. R.W.K. Honeycombe: *Steels-Microstructure and Properties*, Edward Arnold, London, 1980.
2. P. Kolmskog and A. Borgenstam: *Metall. Mater. Trans. A*, 2011, vol. 42A, pp. 3941–51.
3. A. Borgenstam, P. Hedsrtom, M. Hillert, P. Kolmskog, A. Stormvinter, and J. Agren: *Metall. Mater. Trans. A*, 2011, vol. 42A, pp. 1558–74.
4. M. Hillert, L. Hoglund, and J. Agren: *Metall. Mater. Trans. A*, 2004, vol. 35A, pp. 3693–700.
5. G. Spanos, H.S. Fang, and H.I. Aaronson: *Metall. Trans. A*, 1990, vol. 21A, pp. 1381–90.
6. W.C. Cheng and J. Chang: *Mater. Charact.*, 2013, vol. 77, pp. 53–62.
7. G.J. Shiflet, H.I. Aaronson, and J.R. Bradley: *Metall. Trans. A*, 1981, vol. 12A, pp. 1743–50.
8. R.E. Hackenberg and G.J. Shiflet: *Acta Mater.*, 2003, vol. 51, pp. 2131–47.
9. H.J. Lee, G. Spanos, G.J. Shiflet, and H.I. Aaronson: *Acta Metall.*, 1988, vol. 36, pp. 1129–40.
10. F.N. Rhines: *Phase Diagrams in Metallurgy*, McGraw Hill, New York, 1956, pp. 159–272.
11. D.J.S. Cooksey and A. Hellawell: *J. Inst. Met. (Lond.)*, 1967, vol. 95, pp. 183–87.
12. P.R. Howell, J.V. Bee, and R.W.K. Honeycombe: *Metall. Trans. A*, 1979, vol. 10A, pp. 1213–22.
13. K. Campbell and R.W.K. Honeycombe: *Met. Sci.*, 1974, vol. 8, pp. 197–203.
14. W.C. Cheng and S.M. Hwang: *Metall. Mater. Trans. A*, 2011, vol. 42A, pp. 1760–66.
15. W.C. Cheng and Y.C. Li: *Metall. Mater. Trans. A*, 2012, vol. 43A, pp. 1817–25.
16. C.R. Hutchinson and G.J. Shiflet: *Scripta Mater.*, 2004, vol. 50, pp. 1–5.
17. C.R. Hutchinson, R.E. Hackenberg, and G.J. Shiflet: *Acta Mater.*, 2004, vol. 52, pp. 3565–85.
18. J.A. Jimenez and G. Frommeyer: *J. Alloys Compd.*, 2011, vol. 509, pp. 2729–33.
19. A. Schneider, L. Falat, G. Sauthoff, and G. Frommeyer: *Intermetallics*, 2005, vol. 13, pp. 1322–31.
20. K.G. Chin, K.J. Lee, J.H. Kwak, J.Y. Kang, and B.J. Lee: *J. Alloys Compd.*, 2010, vol. 505, pp. 217–23.
21. K.H. Han, J.C. Yoon, and W.K. Choo: *Scripta Metall.*, 1986, vol. 20, pp. 33–36.
22. K.H. Han: *Mater. Sci. Eng. A*, 1995, vol. 197, pp. 223–29.
23. K. Sato, K. Tagawa, and Y. Inoue: *Scripta Metall.*, 1988, vol. 22, pp. 899–902.
24. K. Sato, K. Tagawa, and Y. Inoue: *Mater. Sci. Eng. A*, 1987, vol. 111, pp. 45–50.
25. K. Sato, K. Tagawa, and Y. Inoue: *Metall. Trans. A*, 1990, vol. 21A, pp. 5–11.
26. W.K. Choo, J.H. Kim, and J.C. Yoon: *Acta Mater.*, 1997, vol. 45 (12), pp. 4877–85.
27. M.C. Li, H. Chand, P.W. Kao, and D. Gan: *Mater. Chem. Phys.*, 1999, vol. 59, pp. 96–99.
28. C.S. Wang, C.N. Hwang, C.G. Chao, and T.F. Liu: *Scripta Mater.*, 2007, vol. 57, pp. 809–12.
29. V. Rigaud, D. Daloz, J. Drillet, A. Perlade, P. Maugis, and G. Lesoult: *ISIJ Int.*, 2007, vol. 47 (6), pp. 898–906.
30. H. Ishii, K. Ohkubo, S. Miura, and T. Mohri: *Mater. Trans.*, 2003, vol. 44 (9), pp. 1679–81.
31. K. Ishida, H. Ohtani, N. Satoh, R. Kainuma, and T. Nishizawa: *ISIJ Int.*, 1990, vol. 30 (8), pp. 680–86.
32. W.C. Cheng: *Metall. Mater. Trans. A*, 2005, vol. 36A, pp. 1737–43.
33. W.C. Cheng and H.Y. Lin: *Mater. Sci. Eng. A*, 2002, vol. A323, pp. 462–66.
34. W.C. Cheng, H.Y. Lin, and C.F. Liu: *Mater. Sci. Eng. A*, 2002, vol. A335, pp. 82–88.
35. W.C. Cheng, C.F. Liu, and Y.F. Lai: *Mater. Sci. Eng. A*, 2002, vol. A337, pp. 281–86.
36. W.C. Cheng, C.F. Liu, and Y.F. Lai: *Scripta Mater.*, 2003, vol. 48, pp. 295–300.
37. W.C. Cheng and C.K. Lai: *Scripta Mater.*, 2006, vol. 55, pp. 783–86.
38. V.K. Gorev, V.I. Gurinovich, and V.F. Lisitsyn: *Vest. Akad. Nauk BSSR Ser. Fiz. Tekh.*, 1990, vol. 4, pp. 24–26.

39. C.W. Bale, E. Bélisle, P. Chartrand, S.A. Decterov, G. Eriksson, K. Hack, I.H. Jung, Y.B. Kang, J. Melançon, A.D. Pelton, C. Robelin, and S. Petersen: *CALPHAD*, 2009, vol. 33 (2), pp. 295–311.
40. R.A. Ricks, S.A. Parsons, and P.R. Howell: *Proc. Int. Conf. Solid-to Solid Phase Transformations*, H.I. Aaronson *et al.*, eds., TMS-AIME, New York, 1982, pp. 831–35.